

## **Supplementary information for:**

### **The Paleoproterozoic Otish and Mistassini basins of Quebec, Canada: A record of Superia supercraton breakup and the end of the Lomagundi-Jatuli carbon isotope excursion**

**Malcolm S.W. Hodgskiss<sup>1</sup>, Maxwell A. Lechte<sup>2</sup>, Robert H. Rainbird<sup>3</sup>, Margaret A. Whelan<sup>2</sup>, Robert A. Creaser<sup>4</sup>, William J. Davis<sup>3</sup>, Trond Slagstad<sup>5</sup>, Eduardo T. Mansur<sup>5</sup>, Kalle Kirsimäe<sup>6</sup>, Alex Kovalick<sup>7</sup>, and Andrey Bekker<sup>7,8</sup>**

<sup>1</sup>*Department of Earth Sciences, University of Cambridge, Cambridge CB2 3EQ, United Kingdom*

<sup>2</sup>*Department of Earth and Planetary Sciences, McGill University, Montréal, Quebec H3A 0E8, Canada*

<sup>3</sup>*Geological Survey of Canada, Ottawa, Ontario K1A 0E8, Canada*

<sup>4</sup>*Department of Earth and Atmospheric Sciences, University of Alberta, Edmonton, Alberta T6G 2E3, Canada*

<sup>5</sup>*Geological Survey of Norway, 7491 Trondheim, Norway*

<sup>6</sup>*Department of Geology, University of Tartu, 50411 Tartu, Estonia*

<sup>7</sup>*Department of Earth and Planetary Sciences, University of California, Riverside, California 92521, USA*

<sup>8</sup>*Department of Geology, University of Johannesburg, 2092 Johannesburg, South Africa*

GSA Bulletin, 2025, <https://doi.org/10.1130/B37948.1>.

### Field Photographs:

Most published field photographs of the Mistassini Group and Otish Supergroup are either of poor quality due to digitization or were captured in black and white. Photographs of the studied units are presented below for improved visual documentation of these strata.

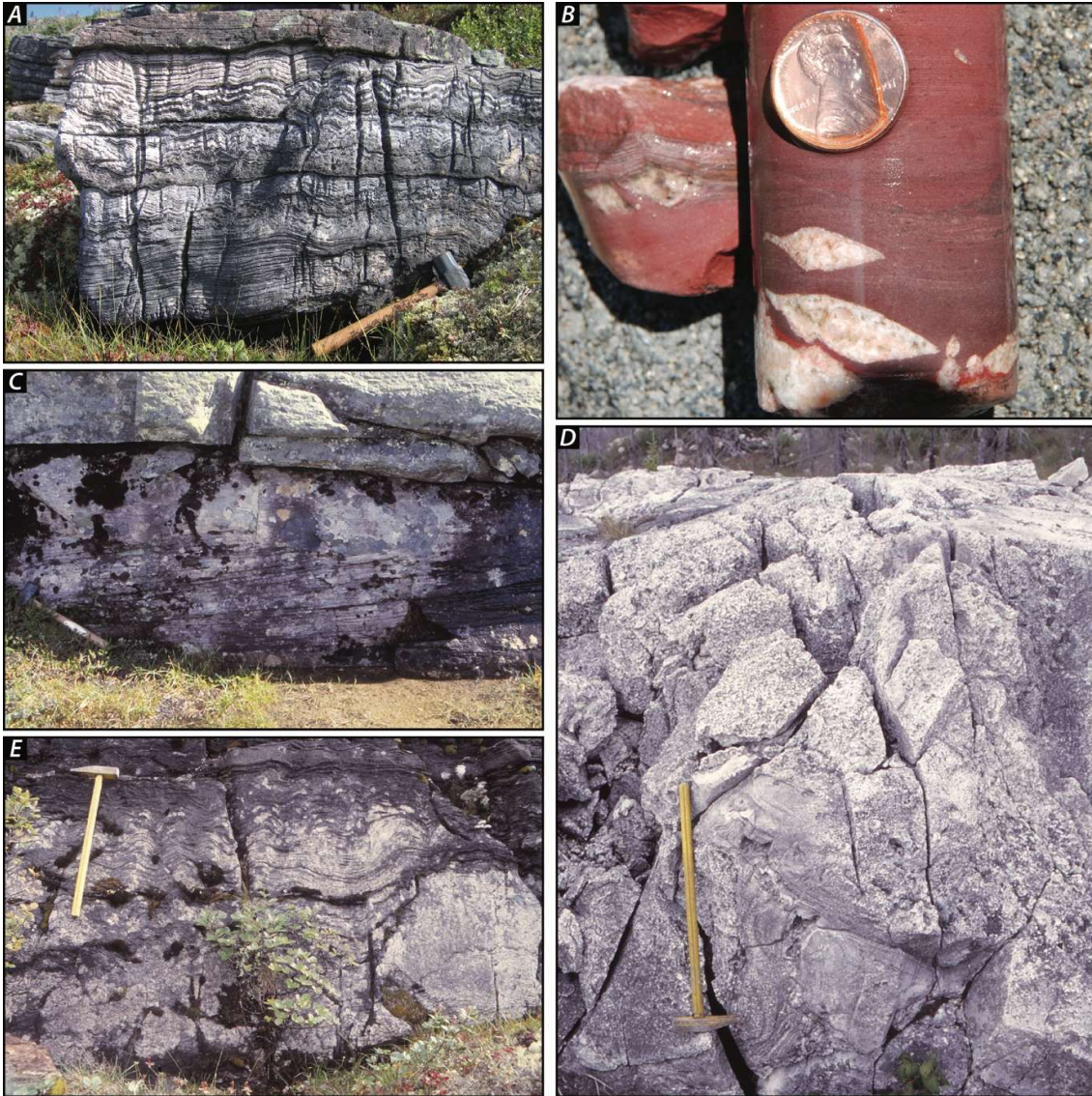


**Figure S1. Photographs of the Gaschet Formation in the Otish Supergroup. A) Wavy and domal stromatolitic dolostone. B) Red beds with sulfate evaporite pseudomorphs. C) Sandstone with large-scale cross-bedding, potentially aeolian in origin. D) Magnesite showing some brecciated clasts. E) Domal stromatolitic dolostone.**





**Figure S2. Photographs of the Papaskwasati and Cheno formations. A) Typical outcrop of the Papaskwasati Formation along a river. B) Trough cross-bedding on a bedding-plane view, Papaskwasati Formation. C and D) Clasts of reworked mudstone in the Papaskwasati Formation. E and F) Dark-grey stromatolitic dolostone of the Cheno Formation.**





**Figure S3. Photographs of the Lower Albanel Formation. A) The Superior craton – Lower Albanel Formation contact. Note distinct quartz-pebble conglomerate layer. B) Regolith developed at the base of the Lower Albanel Formation. C) Very small (sub-mm width) microdigitate stromatolite columns of member A. D) Desiccation cracks in member A. E) Post-depositional brecciation within the member A, potentially related to evaporite dissolution. F and G) Narrow columnar stromatolites of member A that were described by Hofmann (1978).**



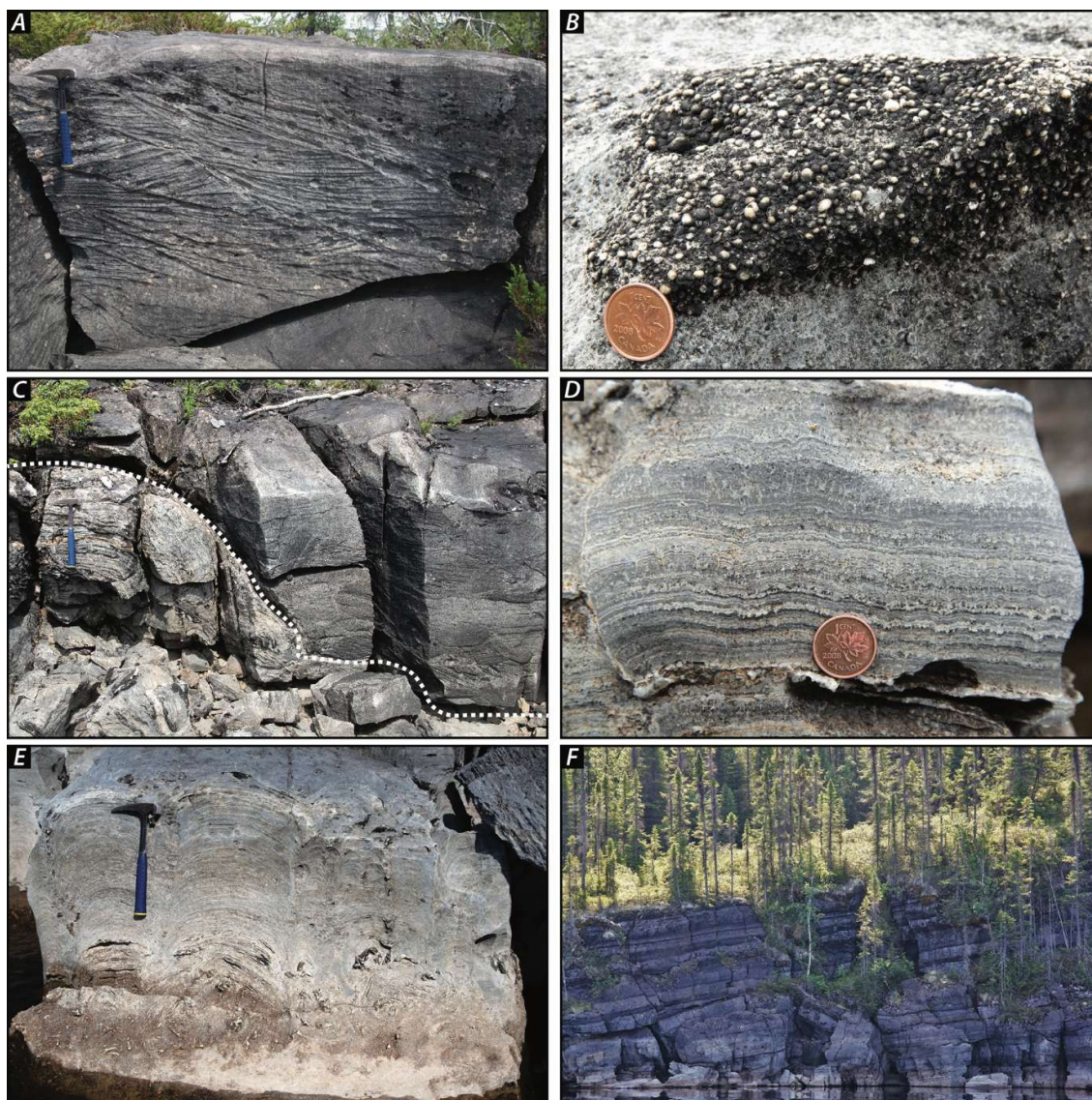


**Figure S4. Photographs of the Upper Albnel Formation. A) Trough cross-bedding in the sandy dolostone member. B) Partially silicified oolite in the sandy dolostone member. C) Domal stromatolite with detrital material and locally derived clasts infilling intercolumnar space in the sandy dolostone member. Dashed line indicates boundary between stromatolites and infill. D) Microdigitate stromatolites in the banded dolostone member. E) Domal stromatolites in the banded dolostone member. F) Prominent ‘striped’ appearance typical of the banded dolostone member.**



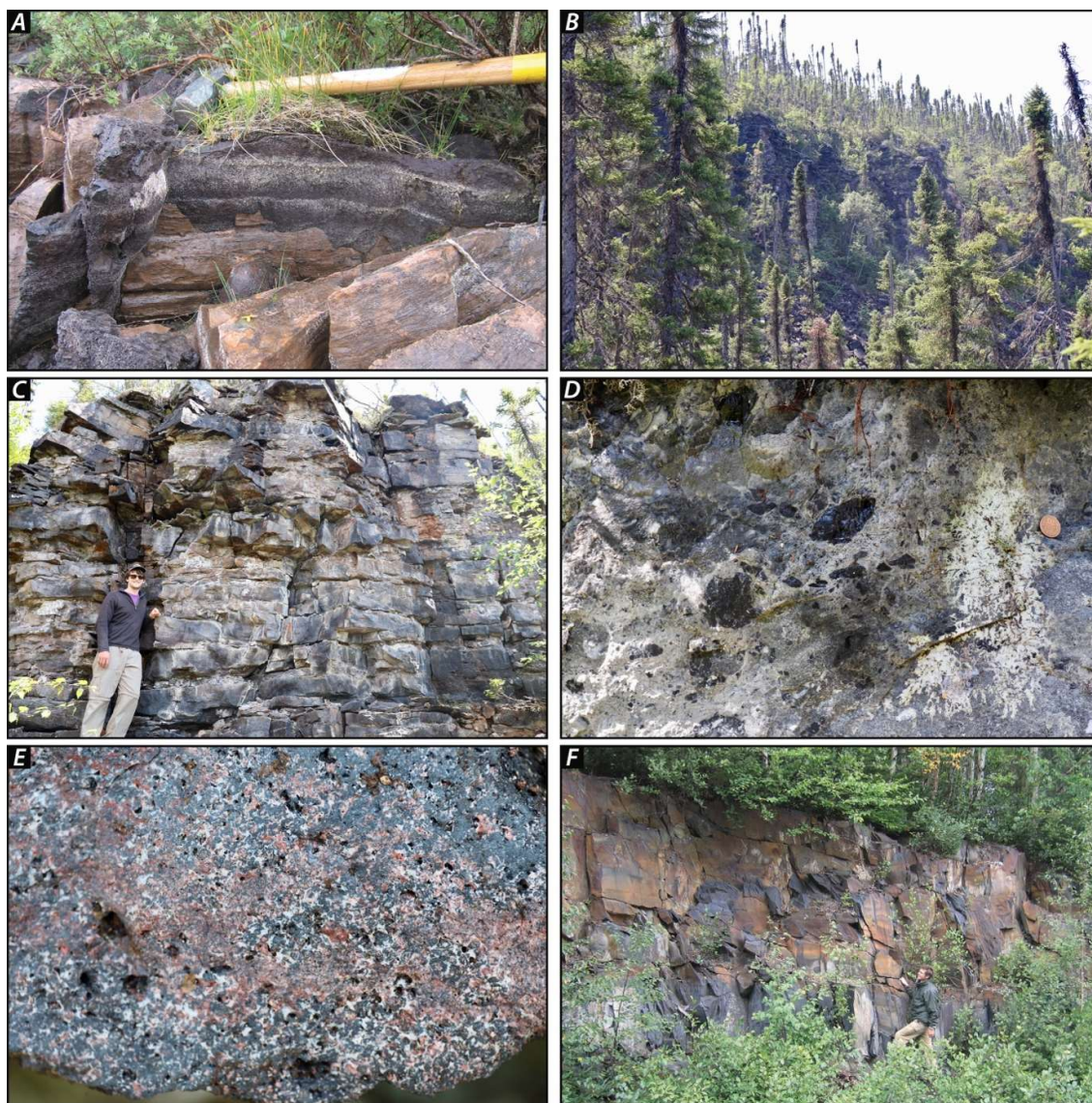


**Figure S5. Photographs of the Temiscamie and Kallio formations. A)** Unconformity at the base of the Temiscamie Formation marked by quartz sandstone infilling cracks and relief in karsted dolostone of the underlying banded dolostone member of the Upper Albanel Formation. Sledgehammer, for scale, is approximately 40 cm long. **B)** The Temiscamie Formation is best exposed on the ridge immediately east of Lake Albanel. **C)** Outcrops at the base of the cliffs east of Lake Albanel of the Temiscamie Formation. Person for scale. **D)** Black chert clasts in the Temiscamie Formation. Canadian penny for scale (diameter = 19 mm). **E)** Granular iron formation of the Temiscamie Formation. The field of view is approximately 5 cm. **F)** Roadcut exposure of the Kallio Formation along Route 167, where samples for Re-Os geochronology were collected. Geologist for scale.



### Petrographic descriptions:

Dolomitized regolith underlying the Mistassini basin carbonates retains some original mineralogy and texture of the underlying bedrock but show dissolution and infill as well as partial mineral replacement. In some cases, feldspar and quartz maintain their crystal structure and original mineralogy (Fig. S6A & S6B) while elsewhere feldspars are partially (Figs. S6C & S6D) to fully replaced (Figs. S6E & S6F) and quartz is heavily corroded (Figs. S6A, S6B, S6E, & S6F). Partial replacement of feldspar with muscovite and carbonate occurs along Carlsbad twinning planes (Figs. S6C, S6D, & S7A-S7D). Finely crystalline chert infills interstitial space between coarser-grained igneous fragments and dolomite and also parallel to jointing in fragments (Figs. S7E & S7F). Cloudy, concentric nodules with ovate and leaf-shaped dolomite crystals around 1 mm in size are common in the regolith (Fig. S8). A later stage dolomite cement fills void space between cloudy dolomite crystals and nodules. Dolomitized rhombic crystals, likely casts of the seed crystals for concentric nodule growth, are commonly in the center of cloudy dolomite nodules (Figs. S7G & S7H & S8C – S8E). The rhombic crystal habit is consistent with either calcite or gypsum as the original mineralogy. Occasionally, replaced seed crystals are twinned (Fig. S8E), closely resembling gypsum swallow-tail twin crystals. Undulating micas (Figs. S7I & S7J; XPL) are likely developed as a replacement of feldspars.

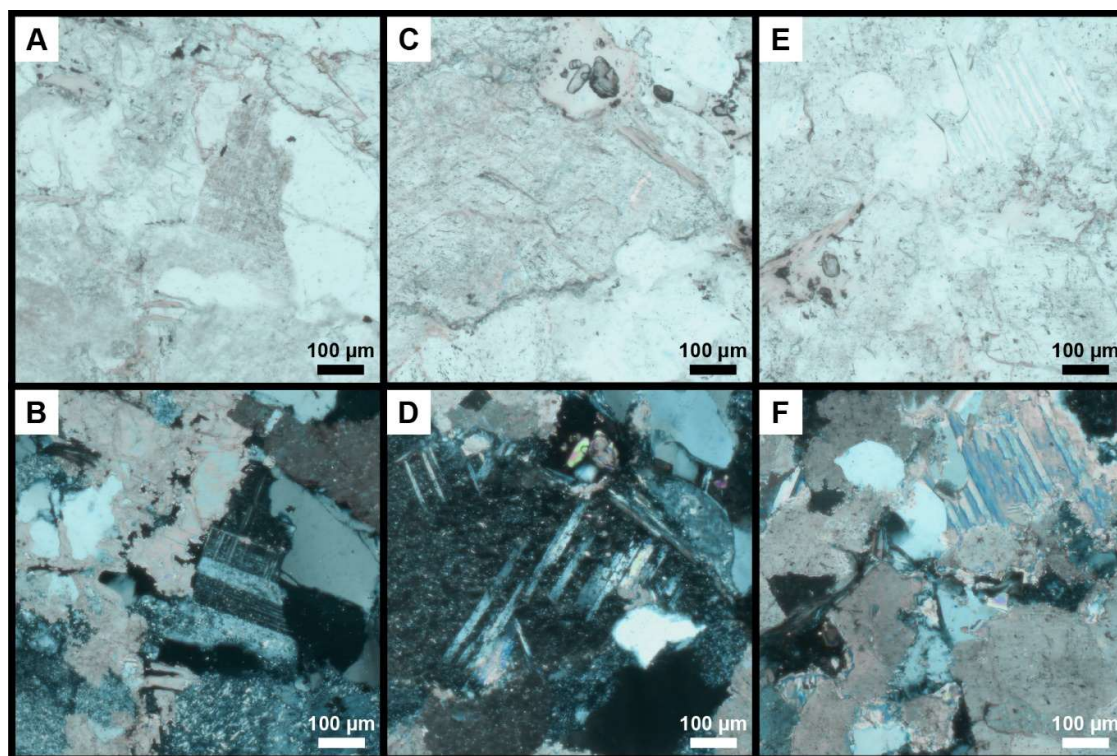


**Figure S6: Photomicrographs of less altered regolith (thin section MM2015C). A & B) Quartz- and feldspar-bearing, locally derived igneous clasts in the regolith with dolomite cement infilling weathered voids and joints in PPL (A) & XPL (B). C & D) Feldspar grains are partially replaced by carbonate and muscovite along Carlsbad twinning planes in PPL (C) & XPL (D). E & F) Fully replaced feldspar grain in the upper-right with corroded quartz surrounded by cloudy dolomite in PPL (E) and XPL (F).**

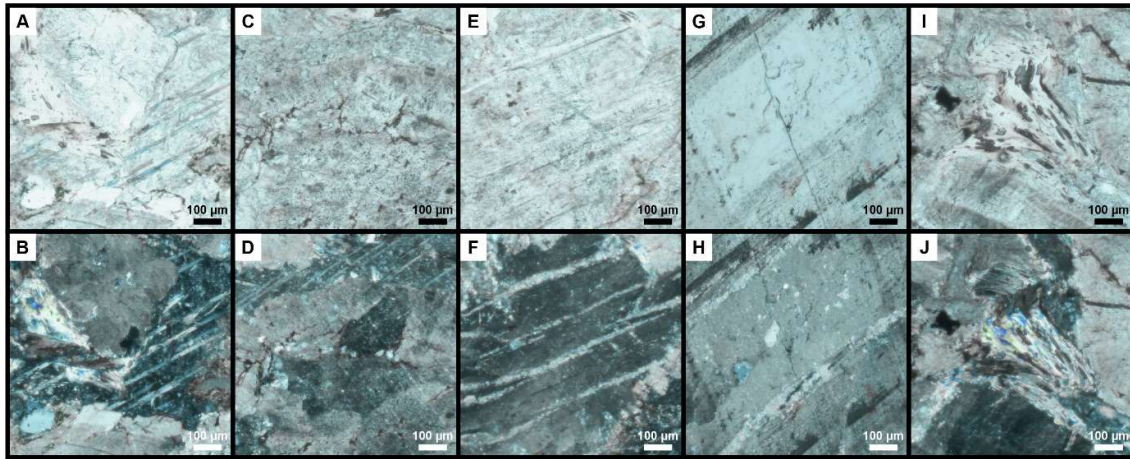


**Figure S7:** Photomicrographs of more altered regolith (thin section MM2104A). A – D) Feldspar is partially replaced by carbonate and muscovite along Carlsbad twinning planes in PPL (A & C) and XPL (B & D). E & F) Finely crystalline chert fills parallel to joints in a feldspar grain in PPL (E) and XPL (F). G & H) Rhombic crystal now dolomitized and crosscut by parallel joints filled with finely crystalline chert in PPL (G) and XPL (H). I & J) Undulating mica crystals between feldspar, quartz, and dolomite grains in PPL (I) and XPL (J).

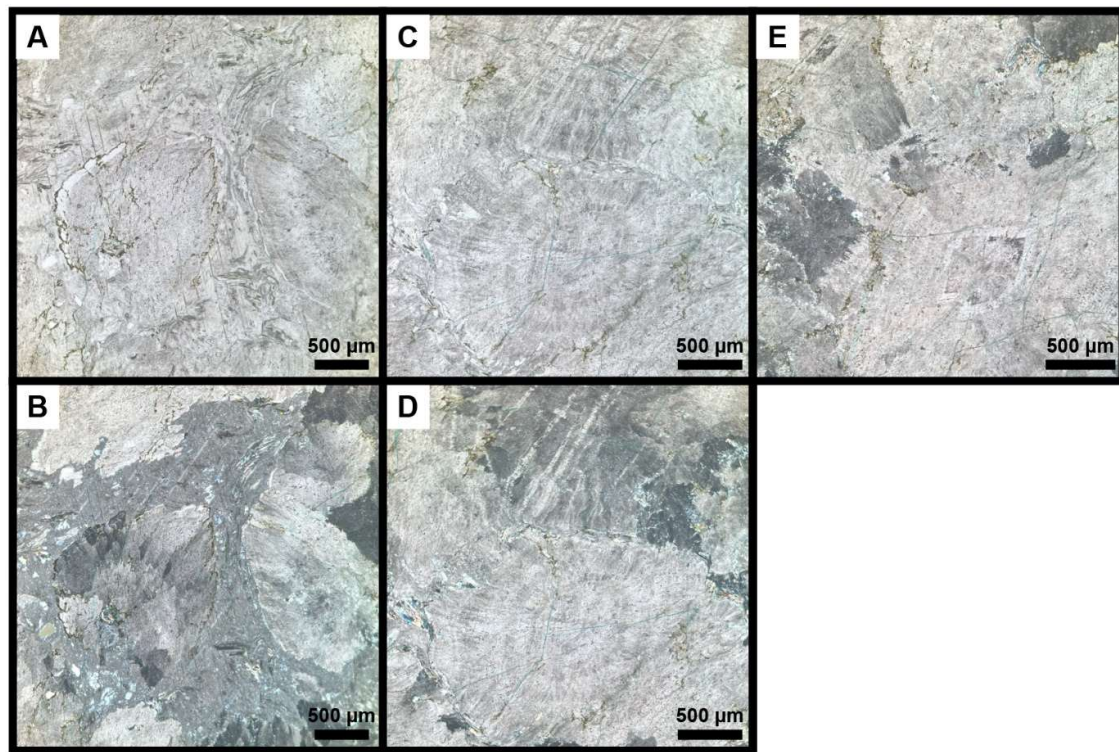


**Figure S8:** Photomicrographs of millimeter-scale concentric nodules with ovate and leaf-shaped dolomite crystals in more altered regolith (thin section MM2104A). A & B) Cloudy dolomite nodules surrounded by later-stage dolomite cement that filled voids in PPL (A) and XPL (B). Note partially dissolved leaf-shaped dolomite crystals to the lower left. C - E) Concentric dolomite nodules with euhedral, rhombic seed crystals in PPL (C) and XPL (D & E). Note that seed crystals commonly have crystal faces at 60° and 120° (C & D) and twinning textures (E) consistent with a possible original gypsum mineralogy.



The immature sandstone at the base of the Lower Albanel Formation (Fig. S9) is composed of poorly sorted, fine to coarse sand-size grains of dominantly quartz (~60-70%), lesser feldspar (~25-30%) (Figs. S9A & S9B), and minor oxides and zircon (Fig. S9C) within a micaceous matrix (dominantly chlorite with some muscovite) infilling space in framework (Fig. S9D). Occasional igneous lithic fragments (Figs. S9E & S9F) are dominantly composed of quartz and feldspar, broadly matching the composition of the finer framework grains. Locally, fine-grained mica is abundant in patches.

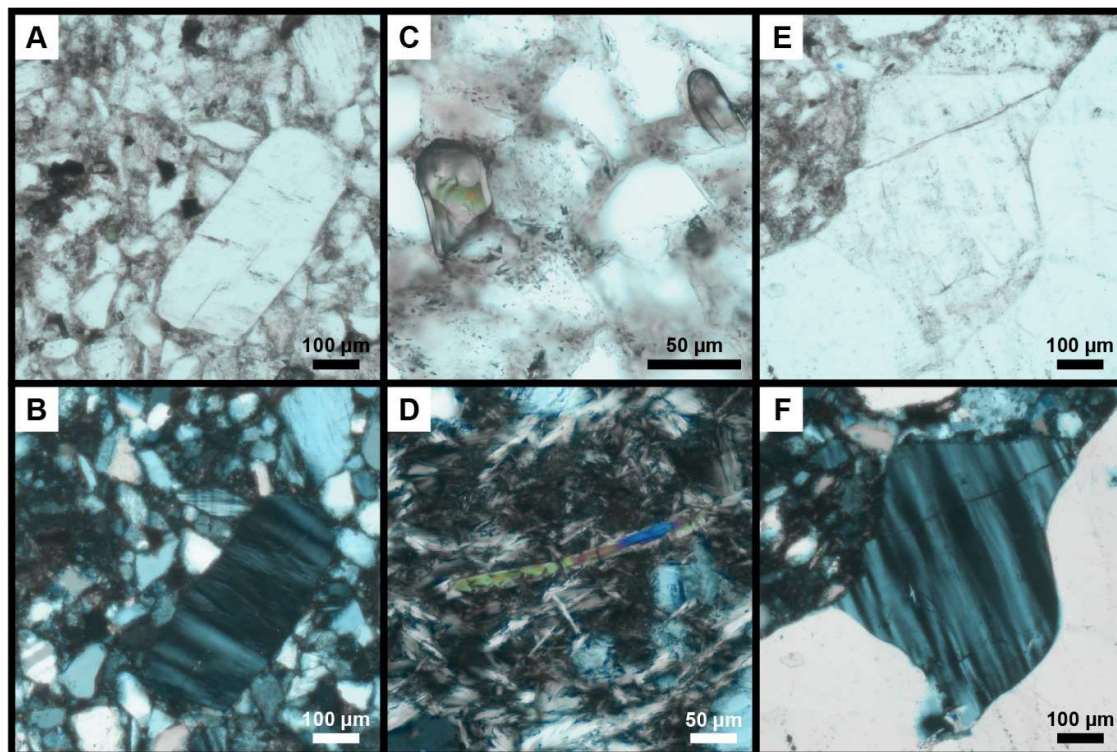


**Figure S9: Photomicrographs of the Lower Albanel Formation sandstone from the Mistassini basin.** *A & B) Sandstone texture showing angular quartz and feldspar framework with minor opaque oxides in PPL (A) and XPL (B). C) Two detrital zircon grains with quartz and minor mica in the sandstone (PPL). D) Mica-rich patch within sandstone predominantly composed of chlorite with some muscovite (XPL). E & F) Part of an igneous lithic fragment within sandstone in the center to lower right of E (PPL) and F (XPL). The lithic fragment is composed of quartz and feldspar similar to those making the framework sand grains.*

Microdigitate stromatolites, developed in member A of the Lower Albanel Formation in the Mistassini basin, are shown in both cross-section (perpendicular to bedding; Figs. S60A – S10C) and plan view (parallel to bedding; Figs. S10D & S10E). While intercolumnar carbonate crystals are somewhat coarser relative to the internal stromatolite structure, indicating some recrystallization, the shape and internal structure of the stromatolites is well-preserved. Stromatolite columns are composed of anhedral sparite (10-50 µm in size) and range from ~200 to 600 µm wide and no more than a few mm in height with lamina thickness ranging from 10 to 20 µm. Columns are seen connected with sagged lamina between them, but also appear to develop alone in some cases. Fine-crystalline chert (>10 µm in size) and coarser anhedral sparite (ranging from ~50 to 500 µm in size) fill intercolumnar space (Fig. S10A, S10B, & S10G). Occasionally, crystals along column exteriors look to be tinted with dark material, particularly along carbonate and chert crystal boundaries. This dark material is likely post-depositional, remobilized pyrobitumen. Stromatolite columns are circular to slightly ovate in plan view (Fig. S10D & S10E) with diameters ranging from 200 to 600 µm and are separated by as little as about 100 µm of intercolumnar space. Micritic carbonate, not associated with stromatolite, is composed primarily of anhedral crystals >5 µm in size with scattered larger crystals up to about 10 µm in size and minor red and opaque oxide crystals >5 µm in size (Figs. S10G & S10H).



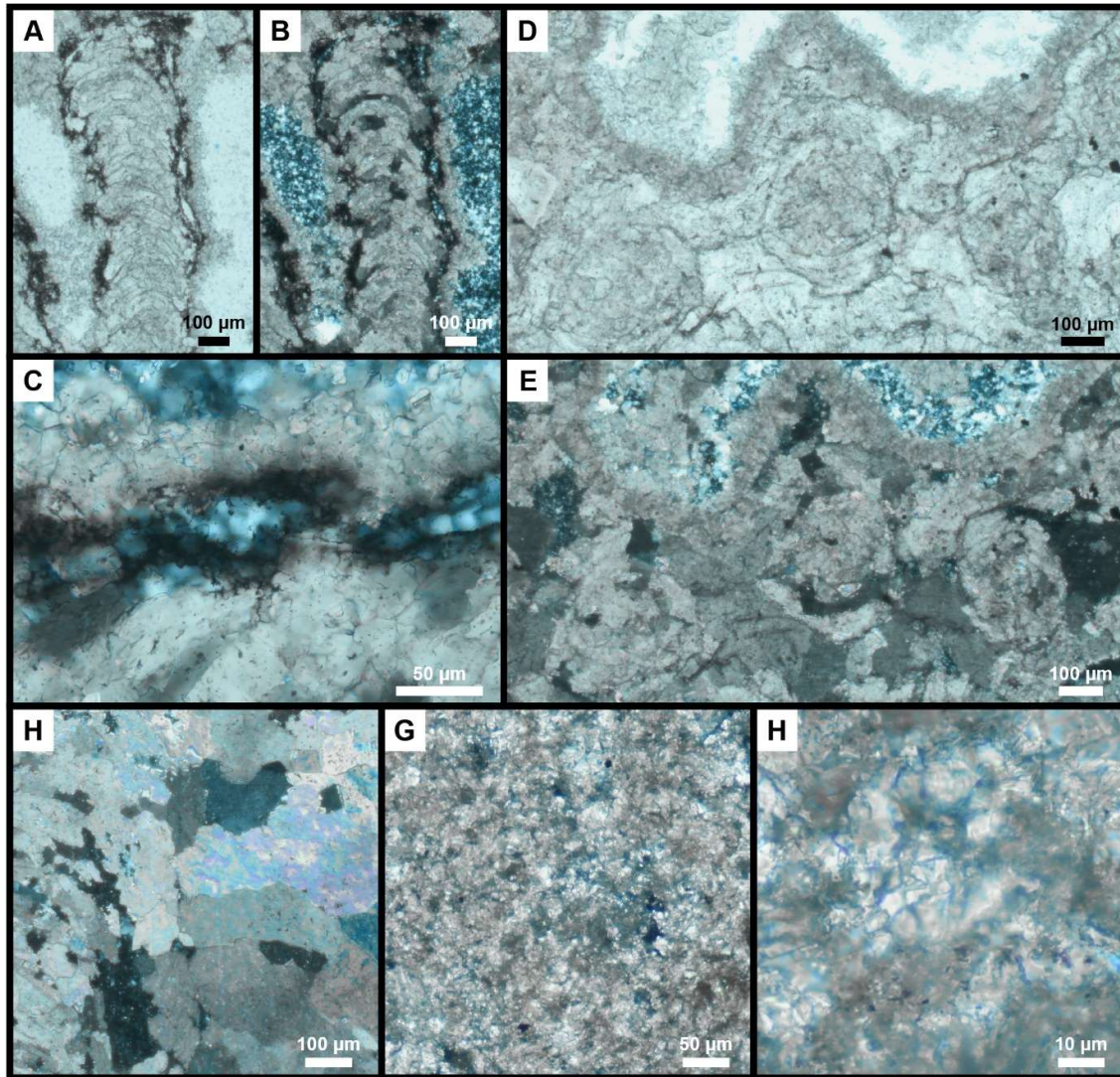


**Figure S10: Photomicrographs of Mistassini microdigitate stromatolites. A & B) Column of microdigitate stromatolites in PPL (A) and XPL (B). Note that the stromatolite column is connected to the neighboring column to the left at the base of the image. Intercolumnar space is filled predominantly with fine-crystalline chert and some carbonate immediately to either side of the columns. C) Higher magnification image showing dark pyrobitumen along the edge of the stromatolite column lining carbonate-chert crystal boundaries shown in the plan view (XPL). D & E) Plan view of stromatolite columns showing 3 columns immediately surrounded by carbonate crystals with fine-crystalline chert at the top of the image filling intercolumnar space in PPL (D) and XPL (E). F - H) Sparite and micrite textures in carbonate. Coarse-crystalline sparite grown alongside a stromatolite column in XPL (F). Micrite texture under low and high magnification in PPL (G & H).**

Stromatolite fragments (Figs S11A & S11B), and quartz (Fig S11C) and feldspar (Fig S11D) grains make up framework in carbonate- and silica-cemented breccia in Member A of the Lower Albanell Formation (Fig. S11). Stromatolite fragments have pyrobitumen lining sparite crystals along the margins of columns similarly to some stromatolite columns in samples where stromatolites are in growth position. Cement in the breccia resembles that of the stromatolitic samples with chert and sparite filling interstitial space within the framework. Dissolution voids in the cement contain euhedral dolomite crystals surrounded by fine-grained chert and pyrobitumen (Figs. S11E – S11F).



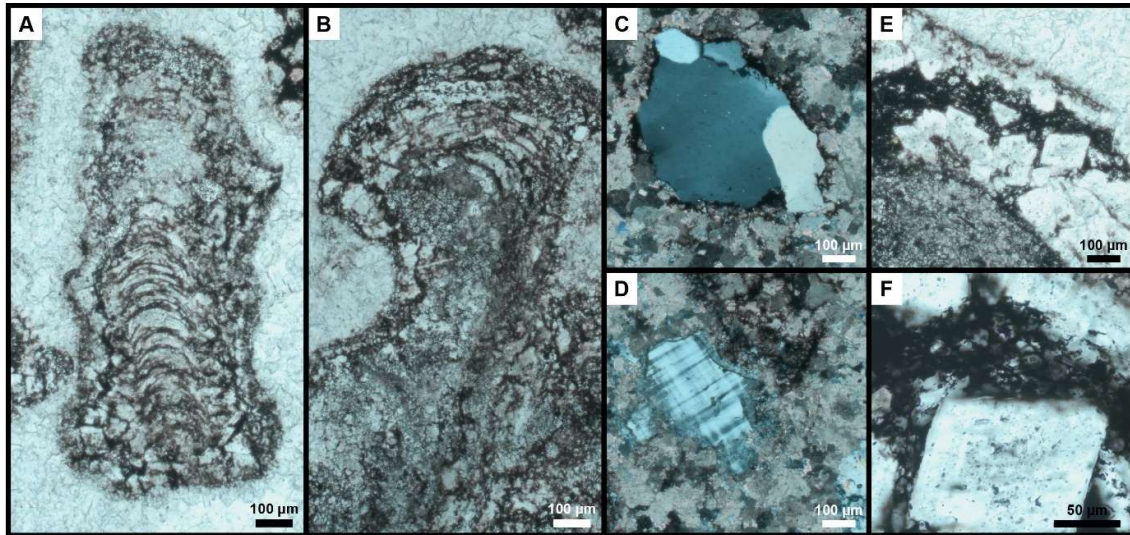


**Figure S11: Photomicrographs of Mistassini carbonate-silica cemented breccia. A & B) Stromatolite fragments within a carbonate-silica cement (PPL) similar to the cement between stromatolite columns that were preserved in life position (Fig. S10). Pyrobitumen lines carbonate crystals along the margins and within the stromatolite clasts. Coarse grained quartz (C, XPL) and feldspar (D, XPL) grains are also present in the framework of the breccia. E & F) Void space, likely formed from partial dissolution, containing euhedral dolomite crystals surrounded by chert and pyrobitumen in PPL.**

Granular iron formation in the Temiscamie Formation (Fig. S12) consists of concentrically coated, coarse sand- to granule-sized grains of chert-jasper, referred to as iron ooids. These iron ooids are subrounded and feature concentric coatings of finely interlaminated hematite, chert and minor siderite and stilpnomelane that are locally overprinted by coarse, euhedral magnetite. The magnetite is sometimes bladed, which may indicate a pseudomorph after siderite. The cores of these granules often feature syneresis cracks, and the cortical laminae locally show evidence for soft-sediment deformation and fracturing. The iron ooid-bearing facies is clast supported with a quartz cement, with grain size sorting and grading locally developed, indicating that the iron ooids formed prior to burial.



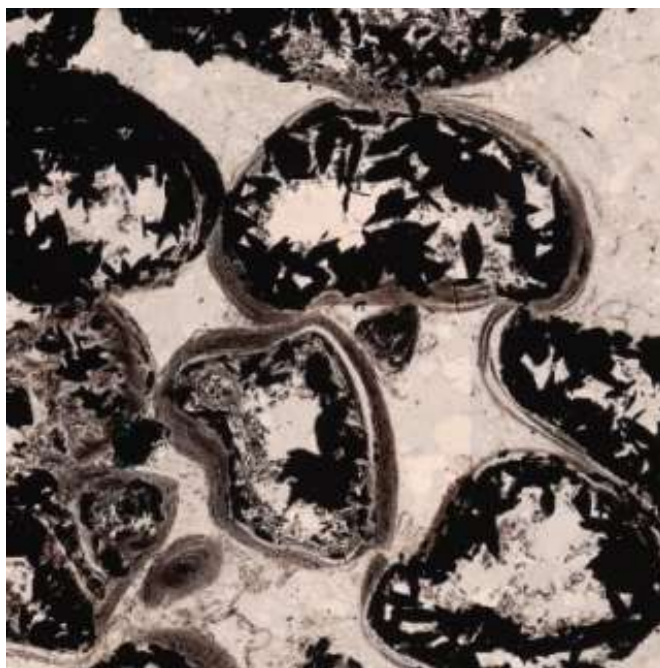


**Figure S12.** Granular iron formation from the Temiscamie Formation exhibits subrounded grains with fine concentric coatings of hematite, chert and minor siderite and stilpnomelane, locally overprinted by coarse, euhedral magnetite. The cores of the granules often contain bladed magnetite, potentially indicating a pseudomorph after siderite. The granules are suspended in a quartz matrix. Field of view is approximately 3 mm.

#### **μXRF element mapping:**

Qualitative X-ray Fluorescence (μXRF) element maps were made using a Bruker M4 Tornado at Norges Teknisk-Naturvitenskapelige Universitet (NTNU; Trondheim, Norway) equipped with a silver X-Ray source and two silicon drift detectors. Analyses were conducted at 50 kV accelerating voltage and 600 μA, with an acquisition time of 2 ms/pixel. The distance between each pixel was 25 μm, and the analytical spot size was 20 μm. Mapping was conducted under a vacuum of 20 mbar. To reduce ‘noise’ in the output images, a 3-pixel averaging filter was applied. The element counts are not calibrated, and element maps should only be assessed individually.

#### **LA ICP MS:**

The *in-situ* U-Pb isotopic measurements were obtained by laser ablation-inductively coupled plasma-mass spectrometry (LA-ICP-MS) at the Geological Survey of Norway (NGU) using a Teledyne-Cetac Analyte Excite Excimer 193 nm laser equipped with a HelEx II two-volume cell and coupled with an Agilent 8900 QQQ-ICP-MS. The LA-ICP-MS tuning parameters were a laser frequency of 6 Hz, a fluence of 2J/cm<sup>2</sup>, and a spot size 15 μm. A dwell time of 40 ms was used for <sup>202</sup>Pb and <sup>204</sup>Pb, 100 ms for <sup>206</sup>Pb, 120 ms for <sup>207</sup>Pb, 20 ms for <sup>208</sup>Pb and <sup>232</sup>U, and 60 ms for <sup>238</sup>U. The gas blank was measured for 20 s before switching on the laser for 20 s, followed by 5 s wash-out period. Ablations were carried out in a He atmosphere and sample aerosol was transported to the ICP-MS by a He carrier gas, with additional Ar added to the He-sample mixture bulb before the plasma torch. Consistent laser parameters were used for all standards and sample measurements in each sequence. The GJ-1 zircon standard (608.5 ± 1.5 Ma; Jackson et al., 2004), used as a calibration standard, was analysed at the beginning and end of each run, and between every 10 analyses. The reference materials 91500 (1065.4 ± 0.3 Ma; Wiedenbeck et al., 1995), Z-6412 (1160 ± 2 Ma; unpublished, GSC Ottawa) and in-house standard Senja (2680 ± 10 Ma; unpublished, NGU) were used to check precision and accuracy.

Data reduction was carried out using the “U-Pb Geochronology” data reduction scheme (“DRS”) in Iolite v. 4. On-peak gas-blank baselines were fit with an “automatic spline” and subtracted from each channel. Approximately 1 s was trimmed from the beginning and end of the selection of data

from each analysis. The GJ-1 zircon was used as primary standard to correct for drift and downhole fractionation, and to normalize  $^{238}\text{U}/^{206}\text{Pb}$  and  $^{207}\text{Pb}/^{206}\text{Pb}$ . Exponential fits to the downhole fractionation trends were used for the downhole correction. Uranium-235 was not measured, and  $^{235}\text{U}$  was therefore calculated from the  $^{238}\text{U}$  signal and a canonical  $^{238}\text{U}/^{235}\text{U}$  of 137.818.

#### SHRIMP:

Analytical methods for SHRIMP U-Pb analyses follow those described by Stern (1997). Zircon were separated using standard crushing (jaw crusher, disc mill) and mineral separation techniques (Wilfley Table, heavy liquids), mounted in epoxy and polished to expose mid-grain. Back scatter electron images were made prior to analyses using a Cambridge Instruments scanning electron microscope. Calibration of U-Pb ratios is relative to the 6266 zircon reference material ( $^{206}\text{Pb}/^{238}\text{U}$  age = 559 Ma), using the  $^{206}\text{Pb}/^{238}\text{U}$  vs.  $^{206}\text{Pb}/^{270}\text{U}$  method (Stern and Amelin, 2003). The target surface was evaporatively coated with 10 nm of high purity Au. An  $^{16}\text{O}^-$  primary beam with a spot size of approximately 17 x 23 mm produced beam currents of ~9 and ~8 nA for session mounts IP420 and IP421, respectively. Individual analyses consisted of five scans of ten mass stations including background, with count rates measured by peak-hopping on a pulse counting electron multiplier system with deadtime of 23 ns. Off-line data processing was accomplished using customized software. Common Pb values included correction for the measured composition of the Au applied to coat the surface. The  $1\sigma$  external uncertainty of individual  $^{206}\text{Pb}/^{238}\text{U}$  ratios reported in the Supplementary Data file incorporate a  $\pm 1.4\%$  and  $\pm 1.0\%$  uncertainty for session mounts IP420 and IP421, respectively. Analyses of GSC reference zircon 1242 over the time interval of the analytical sessions (02/07 to 04/07) yielded a weighted mean  $^{207}\text{Pb}/^{206}\text{Pb}$  age of  $2678.8 \pm 2.4$  Ma ( $n = 3$ ), corresponding well with the accepted value of  $2679.8 \pm 0.2$  Ma (Davis et al., 2019). No mass fractionation was applied.

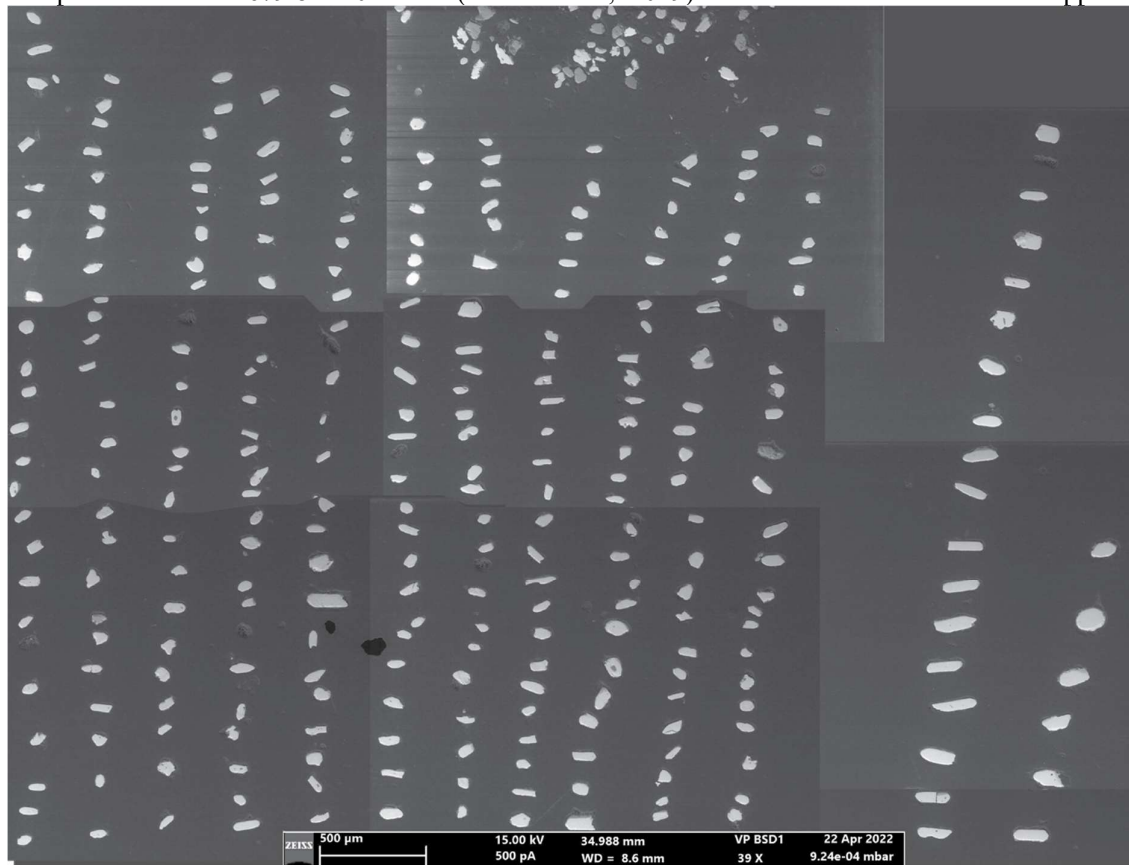


**Figure S13.** Zircons showed little to no zonation under back scatter electron imaging.



## Rhenium – Osmium isotope analyses:

For Re-Os shale dating, approximately 50 g of each shale subsample was broken into small chips without metal contact and powdered in an agate mill. Rhenium–osmium isotope analyses were carried out at the Re-Os crustal geochronology laboratory of the Department of Earth and Atmospheric Sciences, University of Alberta. Between 0.45 g and 0.55 g of powder and a known quantity of a  $^{185}\text{Re}$ – $^{190}\text{Os}$  tracer (UA3) were digested in 8 mL of  $\text{Cr}^{\text{VI}}$ - $\text{H}_2\text{SO}_4$  solution (0.25 g of  $\text{CrO}_3$  per 1 mL of 4N  $\text{H}_2\text{SO}_4$ ) in sealed Carius tubes for 48 hrs (Selby and Creaser, 2003; Kendall et al., 2004). Osmium was separated from the  $\text{Cr}^{\text{VI}}$ - $\text{H}_2\text{SO}_4$  solution by solvent extraction using chloroform, back-extracted into 9 N HBr, and purified by double micro-distillation (Cohen and Waters, 1996; Birck et al., 1997). Rhenium was separated from the  $\text{Cr}^{\text{VI}}$ - $\text{H}_2\text{SO}_4$  solution by anion exchange chromatography (after reaction with  $\text{SO}_2$  gas to reduce  $\text{Cr}^{6+}$  to  $\text{Cr}^{3+}$ ), and further purified by single bead anion exchange chemistry (Selby and Creaser, 2003). Rhenium and Os were loaded onto crimped Ni and Pt filaments, respectively (Kendall et al., 2009). Average laboratory blanks for Re and Os were  $10.3 \pm 2.6$  pg and  $0.16 \pm 0.12$  pg, respectively, with blank  $^{187}\text{Os}/^{188}\text{Os}$  of  $0.19 \pm 0.05$ . Rhenium and Os abundances and isotope compositions were determined by isotope dilution–negative thermal ionization mass spectrometry (ID-NTIMS) on a Micromass Sector 54 mass spectrometer using Faraday collectors in static mode (Re) and a pulse-counting electron multiplier in single-collector peak hopping mode (Os). Metal isotope ratios were obtained by correcting raw Re and Os oxide isotopic ratios for isobaric oxygen interferences. Further corrections were made for instrumental mass fractionation, and blank and spike abundances. In-house standard solutions of Re (ALB-1) and Os (AB-2) were used to assess long-term instrument reproducibility and yielded values consistent with long-term values (see Kendall et al., 2009). Re–Os isochron regressions were performed with IsoplotR (Vermeesch, 2018) using a value of  $1.666 \times 10^{-11} \text{a}^{-1}$  for  $\lambda^{187}\text{Re}$  (Smoliar et al., 1996; Selby et al., 2007),  $2\sigma$  uncertainties for  $^{187}\text{Re}/^{188}\text{Os}$  and  $^{187}\text{Os}/^{188}\text{Os}$  were determined by error propagation and the error correlation coefficient  $\rho$  ('rho') (Kendall et al., 2004).

## References:

- Birck, J.L., Barman, M.R. and Capmas, F., 1997, Re-Os isotopic measurements at the femtomole level in natural samples: *Geostandards Newsletter*, v. 21, p. 19-27.
- Cohen, A.S. and Waters, F.G., 1996, Separation of osmium from geological materials by solvent extraction for analysis by thermal ionisation mass spectrometry: *Analytica Chimica Acta*, v. 332, p. 269-275.
- Davis, W.J., Pestaj, T., Rayner, N., and McNicoll, V.M., 2019, Long-term reproducibility of  $^{207}\text{Pb}/^{206}\text{Pb}$  age at the GSC SHRIMP lab based on the GSC Archean reference zircon z1242: Geological Survey of Canada, Scientific Presentation 111. <https://doi.org/10.4095/321203>
- Kendall, B.S., Creaser, R.A., Ross, G.M. and Selby, D., 2004, Constraints on the timing of Marinoan “Snowball Earth” glaciation by  $^{187}\text{Re}$ – $^{187}\text{Os}$  dating of a Neoproterozoic, post-glacial black shale in Western Canada: *Earth and Planetary Science Letters*, v. 222, p. 729-740.
- Kendall, B., Creaser, R.A. and Selby, D., 2009,  $^{187}\text{Re}$ – $^{187}\text{Os}$  geochronology of Precambrian organic-rich sedimentary rocks: Geological Society, London, Special Publications, v. 326, p. 85-107.
- Selby, D. and Creaser, R.A., 2003, Re–Os geochronology of organic rich sediments: an evaluation of organic matter analysis methods: *Chemical Geology*, v. 200, p. 225-240.
- Stern, R.A., 1997, The GSC Sensitive High Resolution Ion Microprobe (SHRIMP): analytical techniques of zircon U-Th-Pb age determinations and performance evaluation: in *Radiogenic Age and Isotopic Studies*, Report 10, Geological Survey of Canada, Current Research 1997-F, p. 1-31.

- Stern, R.A., and Amelin, Y., 2003, Assessment of errors in SIMS zircon U-Pb geochronology using a natural zircon standard and NIST SRM 610 glass; *Chemical Geology*, v. 197, p. 111-146.
- Vermeesch, P., 2018, IsoplotR: A free and open toolbox for geochronology; *Geoscience Frontiers*, v. 9, p. 1479-1493.
- Wiedenbeck, M.A.P.C., Alle, P., Corfu, F.Y., Griffin, W.L., Meier, M., Oberli, F.V., Quadt, A.V., Roddick, J.C. and Spiegel, W., 1995, Three natural zircon standards for U-Th-Pb, Lu-Hf, trace element and REE analyses; *Geostandards newsletter*, v. 19, p. 1-23.